ACSNANO

www.acsnano.org

ARTICLE

Reversing the Irreversible: Thermodynamic Stabilization of $LiAlH_4$ Nanoconfined Within a Nitrogen-Doped Carbon Host

YongJun Cho, Sichi Li, Jonathan L. Snider, Maxwell A. T. Marple, Nicholas A. Strange, Joshua D. Sugar, Farid El Gabaly, Andreas Schneemann, Sungsu Kang, Min-ho Kang, Hayoung Park, Jungwon Park, Liwen F. Wan, Harris E. Mason, Mark D. Allendorf, Brandon C. Wood,* Eun Seon Cho,* and Vitalie Stavila*

Cite This: https://doi.org/10.1021/acsnano.1c02079

Read Online

ACCESS | Metrics & More | Article Recommendations | Supporting Information

ABSTRACT: A general problem when designing functional nanomaterials for energy storage is the lack of control over the stability and reactivity of metastable phases. Using the high-capacity hydrogen storage candidate $LiAlH_4$ as an exemplar, we demonstrate an alternative approach to the thermodynamic stabilization of metastable metal hydrides by coordination to nitrogen binding sites within the nanopores of N-doped CMK-3 carbon (NCMK-3). The resulting $LiAlH_4$@NCMK-3 material releases H_2 at temperatures as low as 126 °C with full decomposition below 240 °C, bypassing the usual Li_3AlH_6 intermediate observed in bulk. Moreover, >80% of $LiAlH_4$ can be regenerated under 100 MPa H_2, a feat previously thought to be impossible. Nitrogen sites are critical to these improvements, as no reversibility is observed with undoped CMK-3. Density functional theory predicts a drastically reduced Al−H bond dissociation energy and supports the observed change in the reaction pathway. The calculations also provide a rationale for the solid-state reversibility, which derives from the combined effects of nanoconfinement, Li adatom formation, and charge redistribution between the metal hydride and the host.

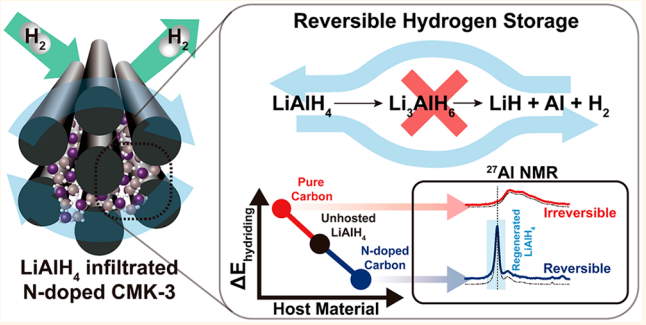

KEYWORDS: *nanoconfinement, metastable materials, metal hydrides, porous carbons, hydrogen storage, coordination chemistry*

The increasing demand for improved materials with complex functionalities requires synthetic approaches that can expand the range of accessible phases through the rational incorporation of metastability into materials design.[1] Metastable materials have become one of the main pillars in advancing novel concepts and transformative technologies in batteries,[2] supercapacitors,[3] piezoelectrics,[4] optoelectronics,[5] and heterogeneous catalysis.[6] In contrast, in the area of materials-based hydrogen storage, metastability has yet to be fully leveraged and in fact has been a major barrier toward practical applications. Metastable hydrogen storage materials, such as NH_3BH_3,[7] metal amidoboranes,[7] $LiAlH_4$,[8] and AlH_3,[9] offer high volumetric and gravimetric energy densities[10] but have unfavorable thermodynamics of hydrogen release and can only be rendered reversible using solution chemistries that require complex and energy intensive off-board regeneration.[7,9,11−15] On top of disadvantageous thermodynamics, these materials often suffer from sluggish hydrogen release kinetics, which has discouraged their consideration as viable on-board vehicular storage candidates.[16]

Nanoscaling is a well-known strategy for improving the properties of metal hydrides, but it has been almost exclusively used to destabilize materials that are too thermodynamically stable, with the most dramatic effects being kinetic rather than thermodynamic in nature.[16−22] Most efforts to date have been focused on nanoconfinement within nanoporous hosts to limit the hydride particle size.[16,23,20,24−27] Carbons and carbon-based materials are by far the most common host materials as they are lightweight and display high chemical and thermal

Received: March 10, 2021
Accepted: May 18, 2021

Table 1. Three Thermal Decomposition Reaction Steps of Bulk $LiAlH_4$ and Their Corresponding Hydrogen Storage Capacities and Reaction Enthalpies[49]

number	reaction	hydrogen storage capacity (wt %)	ΔH(kJ mol^{-1} H_2)
R1	$3LiAlH_4 \rightarrow Li_3AlH_6 + 2Al + 3H_2$	5.3	−10
R2	$Li_3AlH_6 \rightarrow 3LiH + Al + 3/2H_2$	2.6	+25
R3	$LiH + Al \rightarrow LiAl + 1/2H_2$	2.6	

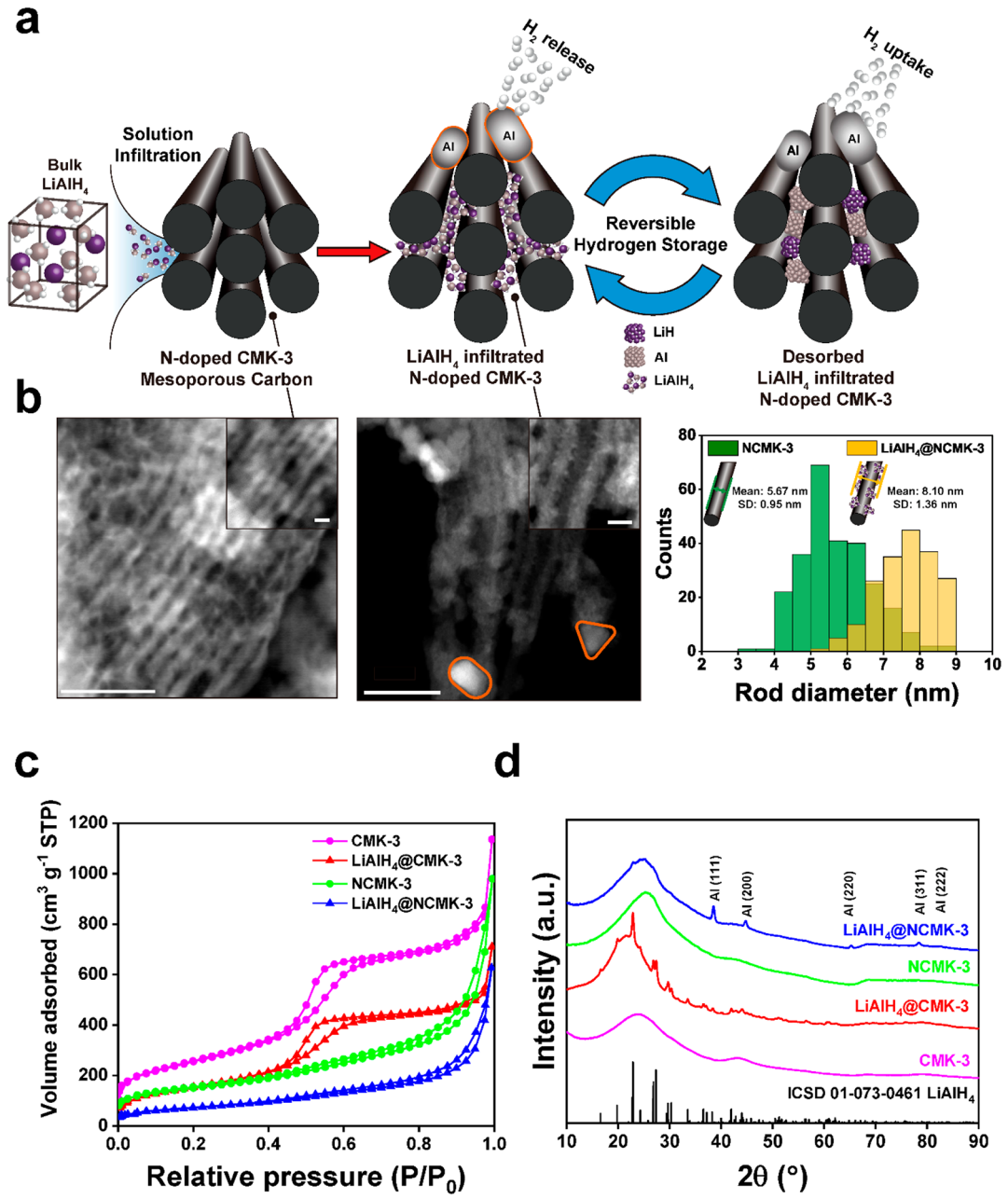

Figure 1. Hydrogen storage mechanism of nanoconfined $LiAlH_4$ in N-doped mesoporous CMK-3 and its structure. (a) Schematic representation of the synthesis and hydrogen storage mechanism of $LiAlH_4$@NCMK-3. (b) High-angle annular dark field scanning transmission electron microscopy (HAADF-STEM) images of N-doped CMK-3 (left) and nanoconfined $LiAlH_4$ in NCMK-3 (middle), and histograms of rod diameters in NCMK-3 and $LiAlH_4$@NCMK-3 and their schematic representations (right). The particles with orange borders represent metallic Al. Scale bars: 50 and 5 nm (inset). (c) Nitrogen adsorption/desorption isotherms at 77 K, and (d) powder X-ray diffraction patterns of nanoconfined $LiAlH_4$ in mesoporous carbon scaffolds.

stability under conditions required to achieve reversible H_2 release.[16,23,28] The pores prevent nanoparticle agglomeration and can also be used to support catalysts that are located in close proximity to the nanoscale guest species. Nielsen *et al.* infiltrated porous carbons with both $NaAlH_4$ and $TiCl_3$ catalyst nanoparticles and found that the onset temperature and

https://doi.org/10.1021/acsnano.1c02079
ACS Nano XXXX, XXX, XXX−XXX

kinetics of hydrogen release are significantly improved due to the favorable synergetic effects between nanoconfinement and catalyst addition.[29] Recent studies by Carr *et al.* show that the incorporation of heteroatoms in carbon affects the kinetics and desorption pathway of the hydride, making the host material an active participant in the reaction process.[30,31] An important advantage of metastable hydrides is that, unlike most binary and complex metal hydrides, very little thermal input is required for hydrogen release. We hypothesize that nanoconfinement can provide a chemical environment similar to the one found in solid adducts of metastable metal hydrides that have shown stabilizing success (for example $LiAlH_4$-dimethyl ether adduct[32]). By analogy, we reason that functionalities capable of inducing charge redistribution between the host and the metal hydride can thermodynamically stabilize metal hydrides and render them reversible.

Here, we report a thermodynamic stabilization concept in which metastable $LiAlH_4$ is nanoconfined within the pores of nitrogen-doped CMK-type carbons. We selected $LiAlH_4$ for this investigation because of its high gravimetric hydrogen content (10.6 wt %) and pure H_2 release upon mild heating.[33,34] In bulk, the thermally induced hydrogen release from $LiAlH_4$ comprises three decomposition steps (Table 1), the first of which is exothermic (-10 kJ mol^{-1} H_2), which makes rehydriding infeasible.[35] In this work, we demonstrate that reversibility in $LiAlH_4$ can be enabled by nanoconfinement within a N-doped carbon scaffold. The resulting nanoconfined $LiAlH_4$ material can be regenerated without resorting to complex solution-phase chemistry, enabling the reconsideration of other high-capacity light metal hydrides that were previously considered unusable for practical applications. These results and the accompanying foundational understanding indicate that the "thermodynamic stabilization" of metastable metal hydrides is a viable approach to hydrogen storage, presenting a suitable strategy for enabling reversibility through guest–host interactions.

RESULTS AND DISCUSSION

Infiltration of $LiAlH_4$ into Functionalized Scaffolds. The preparation of nanoconfined $LiAlH_4$ samples inside the pores of carbon-based scaffolds was achieved *via* the solution infiltration of $LiAlH_4$ freshly recrystallized from diethyl ether. Prior to the infiltration, the mesoporous scaffolds CMK-3 and NCMK-3 were thermally treated at 350–380 °C under a reducing H_2 environment. The hydride nanocomposites are referred to as $LiAlH_4$@CMK-3 and $LiAlH_4$@NCMK-3 depending on the scaffold type (Figure 1a). $LiAlH_4$ was mixed with the appropriate amount of the chosen scaffold in order to achieve a loading of 20 wt % in the final nanocomposite. This loading ensures an efficient and homogeneous infiltration of the hydride inside the pores with minimum pore blockage.

The successful incorporation of $LiAlH_4$ into the pores of CMK-3 and NCMK-3 was confirmed by several bulk and surface-sensitive characterization techniques. First, N_2 isotherms at 77 K indicate a significant reduction in the Brunauer–Emmett–Teller (BET) surface area and total pore volume upon nanoconfinement (Figure 1c). The shape of the isotherms of the mesoporous carbons and their corresponding $LiAlH_4$ loaded composites resemble a type IV(a) isotherm, featuring capillary condensation.[36] Calculated pore size distributions reveal 5–6 nm mesopores in all samples (Figure S1). Both NCMK-3 and $LiAlH_4$@NCMK-3 exhibit a wider pore size distribution than CMK-3, consistent with the higher density of defect sites. $LiAlH_4$ infiltration leads to a reduction of up to 50% in the BET surface area and the total volume for both CMK-3 and NCMK-3 samples (Table S1). The Fourier-transform infrared (FTIR) spectroscopic measurements also indicate the presence of characteristic alanate Al–H stretching and bending modes in $LiAlH_4$@CMK-3 and $LiAlH_4$@NCMK-3. In addition, the FTIR spectra confirm that a significant fraction of –OH functional groups, which could possibly react with $LiAlH_4$, are removed by H_2 cycling treatment prior to infiltration (Figure S2).

The powder X-ray diffraction (PXRD) results also support the nanoconfinement of $LiAlH_4$ in these carbon-based composites. Both as-synthesized composites show only broad or low-intensity reflections of $LiAlH_4$ when compared to a simple physical mixture of NCMK-3 with an equivalent amount of $LiAlH_4$, implying that $LiAlH_4$ confined inside nanoporous hosts exists as nanosized crystallites or as an amorphous phase (Figure S3a).[37] The as-synthesized $LiAlH_4$@NCMK-3 sample exhibits reflections of metallic Al peaks, indicating a partial decomposition of $LiAlH_4$ during infiltration (Figure 1d). Interestingly, ^{7}Li magic angle spinning nuclear magnetic resonance (MAS NMR) reveals that such decomposition generates LiH rather than the expected stable intermediate Li_3AlH_6 (Figure S4). Surface-sensitive X-ray photoelectron spectroscopy (XPS) measurements provide clear evidence that four distinct N functionalities are present in NCMK-3 (Figure S5 and Table S2). Pyridinic N and graphitic N are the major configurations on the surface of the NCMK-3, with minor contributions from oxidized and pyrrolic N groups. Interestingly, the high population of pyridinic nitrogen sites is preserved after hydride infiltration (Table S2 and Supporting Information (SI) Note 1).

HAADF-STEM (high-angle annular dark field-scanning transmission electron microscopy) measurements on nanoconfined samples provide clear evidence of the partial decomposition of $LiAlH_4$ upon infiltration (Figure 1b). In addition, a deposit of small ~1 nm particles was observed on the carbon rods, presumably consisting of $LiAlH_4$. There is a visible structure on the carbon walls in the inset of the infiltrated NCMK-3 shown in Figure 1b. This same surface structure is not observed in the noninfiltrated host material and is thus assigned to the presence of ~1 nm $LiAlH_4$ particles (Figure S6a). The HAADF-STEM line profile of $LiAlH_4$@NCMK-3 shows that the Al signal is uniformly distributed throughout the C, N, and O signals of NCMK-3 and supports a morphology of $LiAlH_4$ uniformly coating the 1D rods of the NCMK-3 host rather than filling the entire available pore space (Figure S6b). Metallic Al nanoparticles with sizes between ~50–100 nm are formed outside the carbon pores, as evidenced from TEM images. The ratio of $LiAlH_4$ and metallic Al quantified by MAS NMR was found to be 0.386, which is a direct result of the metastable nature of $LiAlH_4$, which leads to the partial decomposition of alanate species into Al. The metallic character of Al was confirmed by harmonic peaks from EELS (electron energy loss spectroscopy), indicating a partial decomposition of $LiAlH_4$ upon infiltration (Figure S7). Interestingly, replacing diethyl ether with THF as a solvent for $LiAlH_4$ infiltration still induces a partial decomposition of metastable $LiAlH_4$ (Supporting Information Note 2 and Figure S3b). This is consistent with our preliminary AIMD (*ab initio* molecular dynamics) calculations, which indicate a strong interaction between the N binding sites and $LiAlH_4$, leading to

https://doi.org/10.1021/acsnano.1c02079
ACS Nano XXXX, XXX, XXX–XXX

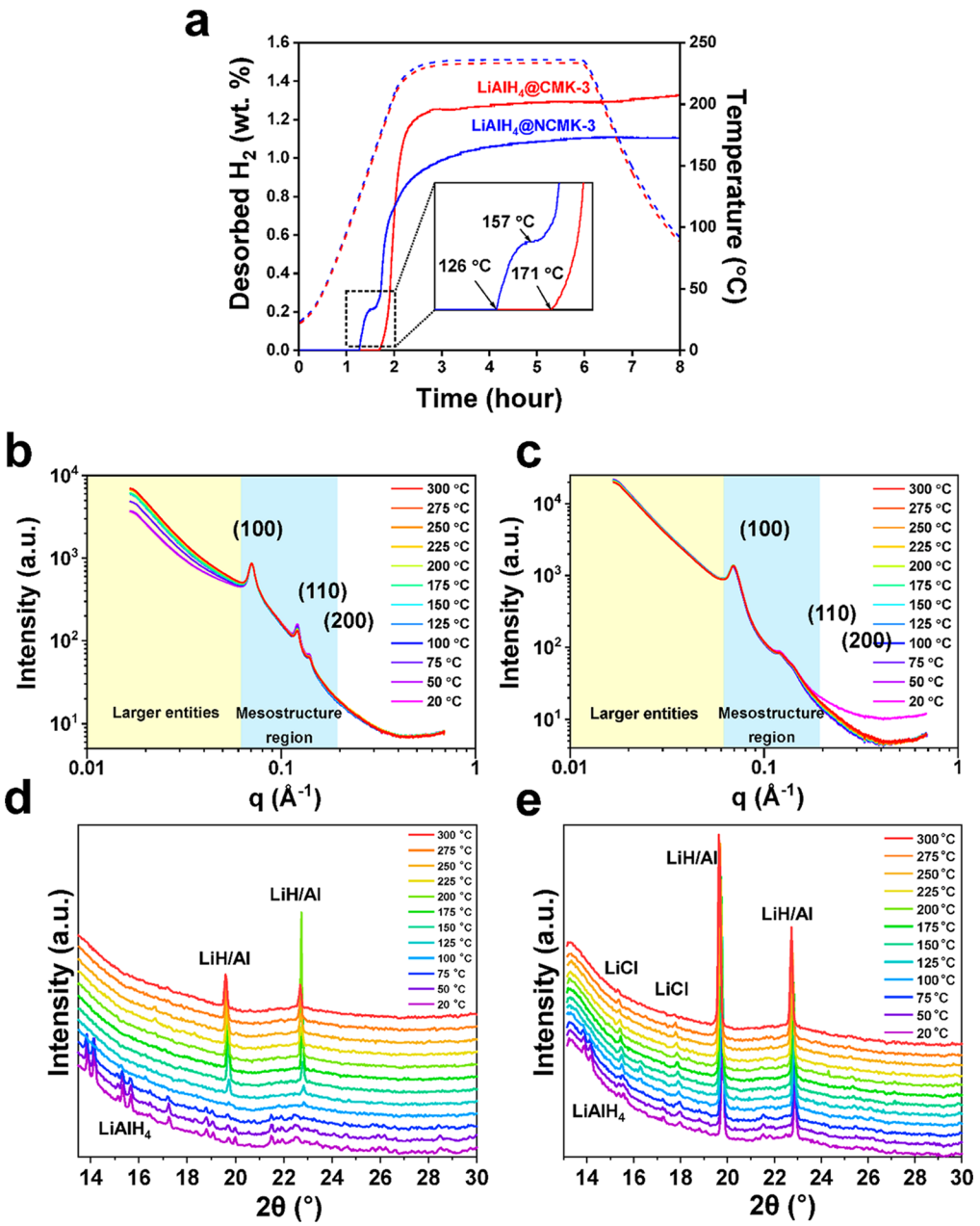

Figure 2. Hydrogen desorption properties and characterization of mesostructures. (a) Hydrogen desorption kinetics curves of $LiAlH_4$@CMK-3 and $LiAlH_4$@NCMK-3. The dashed lines display the temperature profiles for the corresponding desorption curves. *In situ* small-angle X-ray scattering (SAXS) with simultaneous wide-angle X-ray scattering (WAXS) patterns of (b and d) $LiAlH_4$@CMK-3 and (c and e) $LiAlH_4$@NCMK-3 and upon heating from 20 to 300 °C. Three mesostructure peaks from the samples can be assigned to the corresponding (100), (110), and (200) indices based on the hexagonal *P6mm* symmetry of CMK-3 type carbons.[48]

hydride decomposition and spontaneous formation of Li adatoms (*vide infra*) (Figure S8).

Hydrogen Desorption and Absorption. Hydrogen desorption profiles were obtained using the volumetric Sieverts technique and show a lower onset of H_2 desorption temperature for $LiAlH_4$@NCMK-3 compared to $LiAlH_4$@CMK-3 and bulk $LiAlH_4$, implying that the N-functionalities can promote the decomposition of $LiAlH_4$ (Figure 2a and Figure S9). In accordance with the observed self-decomposition of metastable $LiAlH_4$ into LiH and Al in NCMK-3, the capacity of as-synthesized $LiAlH_4$@NCMK-3 is slightly lower than that of $LiAlH_4$@CMK-3. The onset dehydrogenation temperature in $LiAlH_4$@NCMK-3 is as low as 126 °C, 45 °C lower than that in $LiAlH_4$@CMK-3, and 53 °C lower than that in bulk $LiAlH_4$. Interestingly, the dehydrogenation of $LiAlH_4$@NCMK-3 exhibits distinct double steps of hydrogen release with a short transition in the middle of the desorption step at around 157 °C. The origin of the double step is likely associated with various kinetic regimes for $LiAlH_4$ decomposition inside functionalized NCMK-3 pores.

In situ small-angle X-ray scattering (SAXS) with simultaneous wide angle scattering (WAXS) H_2 desorption experiments were used to probe the structural changes of nanoconfined $LiAlH_4$ as a function of temperature (20−300 °C) (Figure 2b−e). These experiments indicate significant structural changes upon heating and formation of distinct

https://doi.org/10.1021/acsnano.1c02079
ACS Nano XXXX, XXX, XXX−XXX

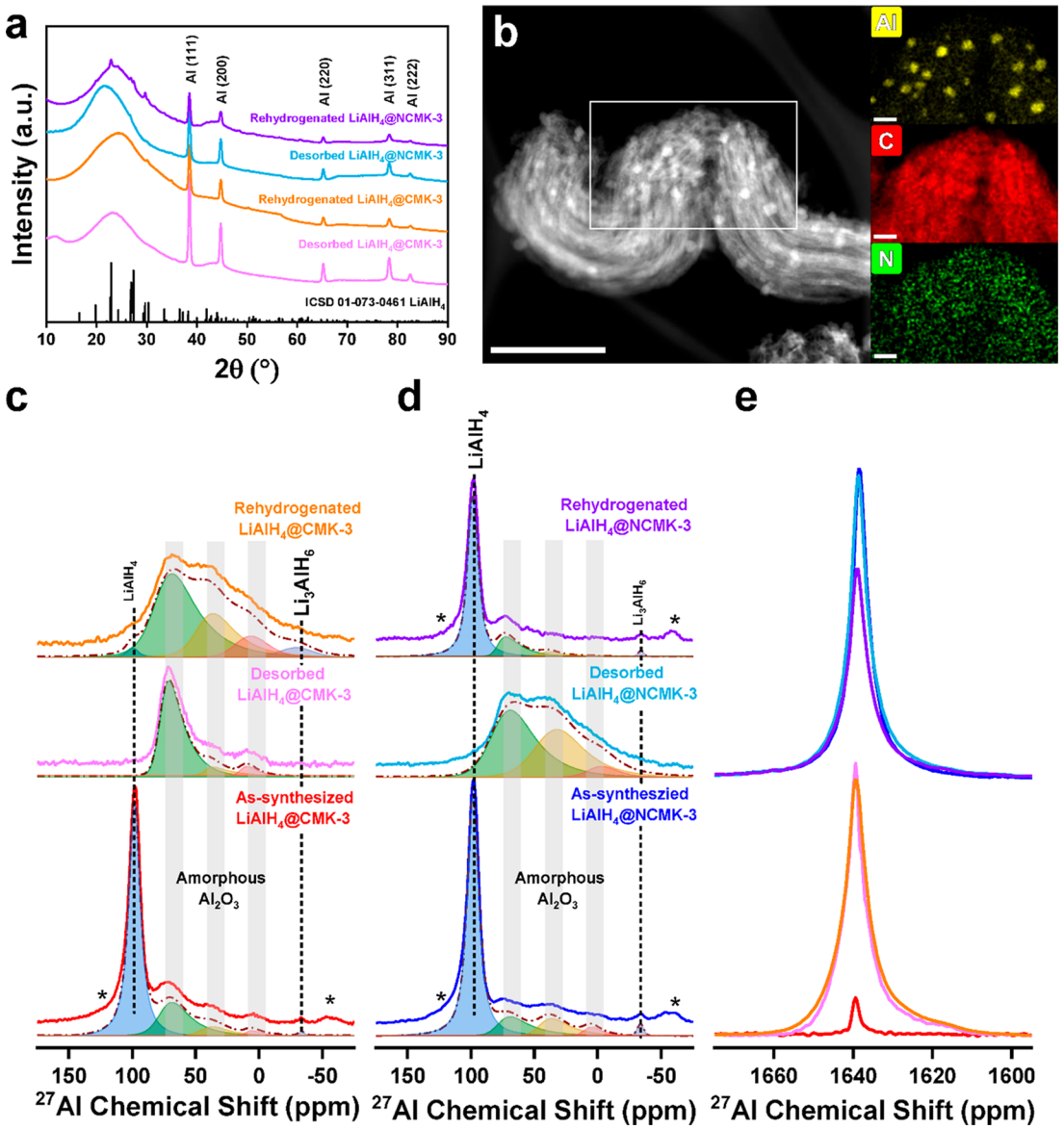

Figure 3. Rehydrogenation of nanoconfined $LiAlH_4$. (a) *Ex situ* powder X-ray diffraction patterns of $LiAlH_4$@CMK-3 and $LiAlH_4$@NCMK-3. (b) HAADF-STEM image and energy dispersive X-ray (EDS) maps of rehydrogenated $LiAlH_4$@NCMK-3. Scale bars: 500 and 100 nm (inset). *Ex situ* ^{27}Al MAS NMR spectra at a low chemical shift range of (c) $LiAlH_4$@CMK-3 and (d) $LiAlH_4$@NCMK-3 and (e) at the metallic Al signal range. In descending chemical shift, the deconvolution components are $LiAlH_4$ (blue), four coordinated Al in amorphous Al_2O_3 (green), five coordinated Al in amorphous Al_2O_3 (orange), and six coordinated Al in amorphous Al_2O_3 (red).

metallic Al peaks. Interestingly, the *in situ* WAXS only exhibits the decomposition of $LiAlH_4$ to LiH/Al without any indications of the stable intermediate phase Li_3AlH_6 upon heating. The intensity in the low-q region of $LiAlH_4$@CMK-3 exhibits an increase at 75 °C and higher, with a simultaneous decrease in the peak area for the three mesostructure peaks (Figure 2b). In contrast, $LiAlH_4$@NCMK-3 displays essentially no change in the small-angle intensity (Figure 2c). At 75 °C and above, where the low-q SAXS intensity of $LiAlH_4$@CMK-3 begins to increase, the WAXS patterns of both $LiAlH_4$@CMK-3 and $LiAlH_4$@NCMK-3 show the decay of $LiAlH_4$ and the formation of Al metal (Figure 2d,e).

The reversible uptake of hydrogen in $LiAlH_4$@NCMK-3 was achieved by treating the dehydrogenated material under 100 MPa H_2 pressure. The PXRD and MAS NMR results support the notion that $LiAlH_4$@NCMK-3 shows reversibility under 100 MPa H_2 pressure at 50 °C, whereas the $LiAlH_4$@CMK-3 composite cannot be rehydrogenated under those conditions.[35] Prior studies have shown that nanoconfinement is as a viable approach to improve the hydrogen storage properties of $LiAlH_4$; however, full reversibility has not been demonstrated.[38−41] Figure 3a displays the PXRD patterns of desorbed and rehydrogenated samples for $LiAlH_4$@CMK-3 and $LiAlH_4$@NCMK-3. The evolution of metallic Al was observed in both N-functionalized and nonfunctionalized samples, with no other crystalline byproducts formed during the decomposition. However, a prominent difference was observed in the rehydrogenated samples. In contrast to $LiAlH_4$@CMK-3, the N-functionalized $LiAlH_4$@NCMK-3 shows broad reflections of $LiAlH_4$ after the rehydrogenation, as well as some residual Al metal peaks, demonstrating the reversible formation of $LiAlH_4$ from LiH and Al under high hydrogen pressure.

The most conclusive evidence for the reversible H_2 uptake and release from $LiAlH_4$@NCMK-3 was obtained from MAS

https://doi.org/10.1021/acsnano.1c02079
ACS Nano XXXX, XXX, XXX−XXX

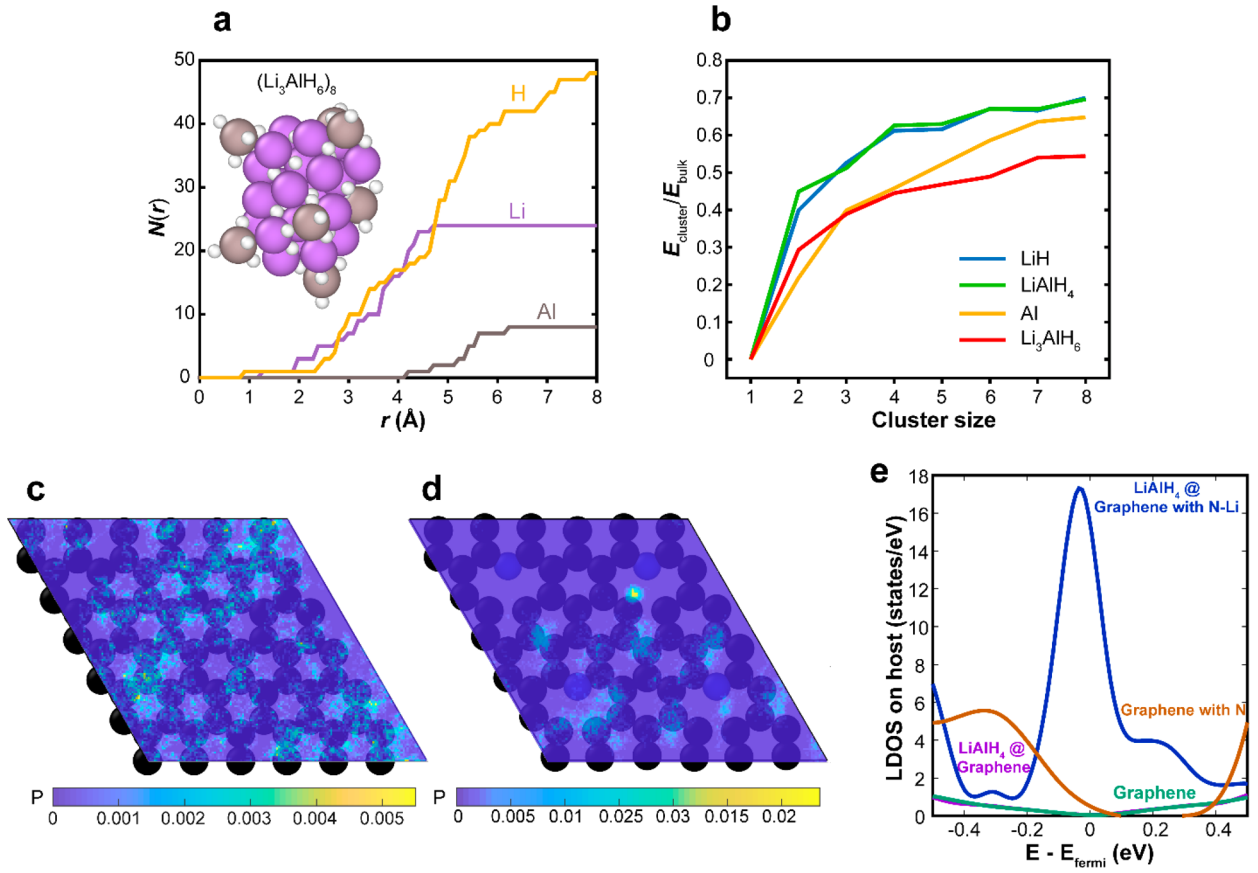

Figure 4. Theoretical study regarding clusters of $LiAlH_4$-related compounds and $LiAlH_4$−scaffold interactions. (a) Integrated atomic number density $N(r)$ as a function of distance r from the center of mass of an isolated $(Li_3AlH_6)_8$ cluster. The inset shows the corresponding relaxed cluster geometry. (b) Ratio of molar formation energies (referenced to an isolated molecular unit) of isolated clusters of varying size versus bulk compounds ($E_{cluster}/E_{bulk}$) for key reaction intermediates. (c and d) Probability density of Li atoms in a $(LiAlH_4)_8$ cluster on (c) pristine graphene versus (d) graphene with a pyridinic N defect, averaged over the AIMD simulation trajectory. (e) Electronic density of states of pure graphene and pyridinic N-doped graphene before and after incorporation of $(LiAlH_4)_6$. H, Al, Li, C, and N atoms are shown in white, gray, purple, black, and blue, respectively.

NMR, a technique that provides information about all species present in the sample, including the amorphous ones. Typical ^{27}Al MAS NMR peaks for the tetrahedral Al in $LiAlH_4$ were observed at 98 ppm in both as-synthesized $LiAlH_4$@NCMK-3 and $LiAlH_4$@CMK-3, indicating successful hydride incorporation (Figure 3c−e).[42] After H_2 desorption, Al peaks from four-coordinated $LiAlH_4$ (and the remaining six-coordinated Li_3AlH_6) disappear in both samples, indicating complete decomposition into LiH and metallic Al. Upon rehydrogenation, the $LiAlH_4$ peak at 98 ppm is only observed in $LiAlH_4$@NCMK-3, which confirms that the rehydrogenation reaction only occurs in $LiAlH_4$@NCMK-3, in agreement with the PXRD results. These results confirm that metallic Al is the only Al-containing decomposition product upon desorption (Figure 3b) since signals for the intermetallic LiAl decomposition products that occur at 380 and 176 ppm were not detected. The corresponding ^7Li NMR data (Figure S10) also show that the regeneration proceeds from LiH to $LiAlH_4$ without any indications of Li_3AlH_6 or intermetallic LiAl phases. Encouragingly, the integration of the ^{27}Al MAS NMR peaks reveals that, during rehydrogenation, ∼80% of the initially infiltrated $LiAlH_4$ was regenerated. In contrast, the ^{27}Al and ^7Li MAS NMR results for the $LiAlH_4$@CMK-3 samples revealed the same reaction products (LiH and Al) and impurity peaks (Al_2O_3), but the $LiAlH_4$ peak was absent after rehydrogenation, confirming that the reaction is only reversible when using the NCMK-3 scaffold.

The HAADF-STEM images of the rehydrogenated composite show small Al species inside the NCMK-3 scaffold, in addition to the large metallic Al particles. Figure 3b shows HAADF-STEM images and energy dispersive X-ray spectra (EDS) of the rehydrogenated $LiAlH_4$@NCMK-3 sample. As expected from the PXRD patterns, the large 50−100 nm Al particles were detected outside the pores of the NCMK-3 scaffold. Both Al-rich areas (at the Al particles) and other low-concentration Al areas were investigated for comparison, and the Al EDS signal was also detected from the background area, implying that species other than metallic Al exist inside the pores (Figure S11), consistent with the ^{27}Al and ^7Li MAS NMR results.

Origin of Reversibility and Altered Reaction Pathway. Collectively, the experiments suggest three potentially governing physical effects: (1) the nanoconfinement of $LiAlH_4$ in CMK-3 and NCMK-3 destabilizes the Li_3AlH_6 intermediate upon H_2 release; (2) Li adatoms form on nitrogen binding sites in NCMK-3 upon infiltration and affect the subsequent chemical reactivity of $LiAlH_4$; and (3) both factors contribute to reversible $LiAlH_4$ regeneration in NCMK-3 upon applying hydrogen pressure. Each of these effects was explored further using carefully controlled *ab initio* simulations,

https://doi.org/10.1021/acsnano.1c02079
ACS Nano XXXX, XXX, XXX−XXX

which confirm the experimental observations and offer additional insights into the origins of the observed behavior.

To explore the effect of confinement on the destabilization of Li_3AlH_6, we generated cluster models with varying sizes to evaluate the stability of all relevant compounds for each size. The AIMD of LiH, Al, Li_3AlH_6, and $LiAlH_4$ nanoclusters ranging from one to eight formula units was run, with the larger sizes approximating the real dimensions of the nanoconfined system (Figure S12). As shown in the equilibrium structure in the inset of Figure 4a, the AlH_6^{3-} units that are the building blocks of bulk Li_3AlH_6 become intrinsically unstable at the nanoscale, converting instead into AlH_4^- units. In contrast, the other tested species at the nanoscale retain their general molecular structure. A closer examination of the integrated radial atomic distributions reveals that the Li_3AlH_6 clusters of various sizes (1−8 formula units) consist of AlH_4^- units segregated on the surface and a core composed of an atomic-scale mixture of LiH and Al (Figure 4a). The spontaneous atomic-scale mixing of LiH and Al was further confirmed by complementary simulations of individual clusters in close proximity (Figure S13).

The Li_3AlH_6 destabilization at the nanoscale could be a response to the breakdown of intermolecular cohesion. To probe this, we computed the formation energy of each compound cluster from an assembly of individual molecular formula units (*i.e.*, cluster size of unity). As shown in Figure 4b, many larger clusters of Li_3AlH_6 are required to recover the stabilizing effect of bulk cohesion compared to the other reaction compounds. We can therefore conclude that the Li_3AlH_6 phase is significantly destabilized upon nanosizing, consistent with the lack of any indication of Li_3AlH_6 in experimental data. Instead, the system bypasses Li_3AlH_6, and hydrogenation and dehydrogenation cycles only involve $LiAlH_4$ and LiH phases.

This inhibition of the Li_3AlH_6 phase is an important key for understanding the hydrogen release from $LiAlH_4$@NCMK-3. We conclude that the two-step decomposition of $LiAlH_4$ is attributable to hydrogen release from nanoconfined $LiAlH_4$ in various chemical environments inside the pores of NCMK-3. The overall process can be represented as $LiAlH_4 \rightarrow LiH + Al + 3/2H_2$ on the basis of the following observations. Unlike other observed desorption profiles that show a gradually increasing desorption rate, the first decomposition step of $LiAlH_4$@NCMK-3 displays fast linear desorption, indicating an accelerated hydrogen release from $LiAlH_4$ nanoparticles (Figure 2a). Even if thermal decomposition involves a transient Li_3AlH_6 phase, there is no indication that this phase accumulates in appreciable amounts during hydrogen desorption or absorption; this conclusion is supported by the highly sensitive ^{27}Al MAS NMR spectroscopy results. It is possible that the decomposition of Li_3AlH_6 becomes much faster compared to bulk by catalysis on carbon surfaces and/or by nanoconfinement,[16,28] which results in a net single-step $LiAlH_4$ decomposition. This experimental observation is consistent with our theoretical prediction that the H_2 desorption of $LiAlH_4$ nanoparticles in $LiAlH_4$@NCMK-3 bypasses the stable Li_3AlH_6 phase. Notably, this is similar to the observed decomposition behavior of $NaAlH_4$ at a nanoscale.[31,37,43]

Another factor potentially in play is the nature of the interaction between $LiAlH_4$ and carbon scaffolds. We ran additional AIMD simulations of $LiAlH_4$ clusters on planar pristine graphene and pyridinic N-doped graphene sheets to approximate scaffold walls in CMK-3 and NCMK-3 (Figure S14). Although there is evidence for graphitic and pyrrolic defects in the scaffold (Figure S5), we focused on the pyridinic defects to explore the interaction with $LiAlH_4$ since the higher degree of excess charge localization on pyridinic defects is likely to have a greater overall impact on the reaction. On pristine graphene (broadly representative of CMK-3), the AIMD simulations reveal little change in the structure of the $LiAlH_4$ cluster. However, in the presence of the pyridinic N defect, Li atoms are drawn away from the cluster toward the graphene surface to coordinate with N. Using Li energy references derived from bulk state $LiAlH_4$, LiH, Al, and gaseous H_2, it was determined that the Li coordination reaction is exergonic and thus irreversible after initial infiltration (Figure S14). This coordination also anchors the cluster to the surface, suggesting a strong interaction and indicating an impact well beyond the single Li adatom involved in the Li−N bond formation (Figure 4c,d).

To further investigate the nature of the Li−N interaction, we analyzed the electronic structure of pristine graphene and pyridinic N-doped graphene models in the presence of $(LiAlH_4)_6$ clusters (Figure 4e). On pristine graphene, the addition of $LiAlH_4$ has little effect on the electronic density of states (DOS). On the contrary, if pyridinic nitrogen is present, the localized state associated with the N atom exhibits a pronounced chemical change upon the incorporation of $LiAlH_4$, delocalizing its charge. This different behavior of the two model carbon hosts can be rationalized in part on the basis of the low DOS of graphitic derivatives in the vicinity of the Fermi level, which requires a large energetic penalty for charge redistribution. The presence of pyridinic N removes this DOS limitation, permitting the host to take a more direct role in the process. The positive impact of N on the otherwise low graphitic DOS has been invoked to rationalize improved kinetics in other carbon-confined hydrogen storage materials[30] and closely parallels the known role of N in overcoming DOS limitations in carbon materials for electrochemical energy storage.[44]

Notably, the dominant effect of $LiAlH_4$ incorporation on the DOS of N-doped graphene is well-captured by the simple approximation of a single adsorbed Li atom on that surface (Figure S15). This confirms that the Li−N interaction dominates the essential physics and that Li atoms are indeed drawn away from the primary cluster (see Figure S15 for a corresponding map of the charge density redistribution). Using this simple Li-adsorbed model, we were also able to reproduce an observed shift in the experimentally measured X-ray absorption spectrum (XAS) of N K-edge in neat NCMK-3, as-synthesized, desorbed, and rehydrogenated $LiAlH_4$@NCMK-3. As shown in Figure S16, the predicted Li−N chemical interaction leads to an energy shift in the computed XAS results that is quantitatively consistent with the measured spectra. This same XAS energy shift was detected under all measured conditions, supporting the conclusion that Li−N coordination is an irreversible process and confirming that Li adatoms near pyridinic N defects introduced during infiltration remain bound in the following (de)hydrogenation cycles.

The retention of Li at the N sites is expected to further impact the reaction cycle, including reversibility. To explore this effect further, a set of models containing one Li atom anchored to each N site was generated, with additional $(LiH + Al)_6$ and $(LiAlH_4)_6$ incorporated separately as the reactant and product, respectively. From Figure 5, the presence of the

https://doi.org/10.1021/acsnano.1c02079
ACS Nano XXXX, XXX, XXX−XXX

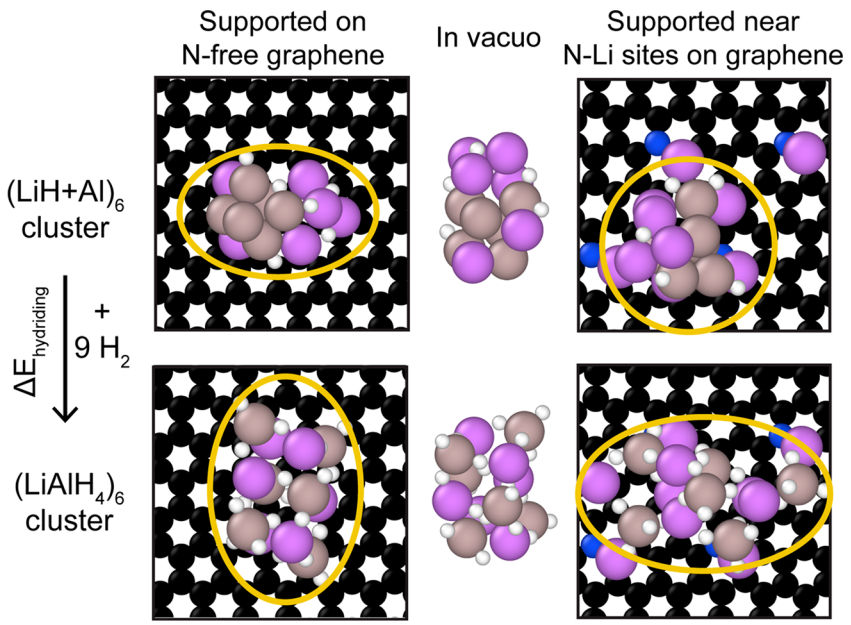

Figure 5. Relaxed structures of $LiAlH_4$-related compounds with different carbon hosts: $(LiH+Al)_6$ (left panels) and $(LiAlH_4)_6$ (right panels) clusters on pristine pristine graphene (top panels) versus the pyridinic defect (bottom panels). H, Al, Li, C, and N atoms are shown in white, gray, purple, black, and blue, respectively.

anchored Li adatoms on the N sites significantly alters the structural configurations of the clusters, enhancing spreading along the surface to maximize the Li−N interactions. On the basis of these models, the thermodynamic impact was assessed. Note that with the small cluster sizes accessible within our model (chosen to facilitate manageable structural sampling while capturing the essential effect of cohesive interactions on phase stability), all computed $\Delta E_{hydriding}$ are exothermic regardless of the presence or nature of hosts. However, a more meaningful comparison can be obtained by instead examining the effect on the hydriding reaction energy, $\Delta E_{hydriding}$, for a given cluster size. For the $(LiH+Al)_6$ to $(LiAlH_4)_6$ conversion under H_2, the presence of Li adatoms on N defect sites lowers $\Delta E_{hydriding}$ by 8 kJ mol^{-1} H_2 compared to pristine graphene (Figure 5) and by 4 kJ mol^{-1} H_2 compared to unsupported clusters *in vacuo*. As the effect on $\Delta E_{hydriding}$ is caused by strong interfacial interactions between the N-doped host and $LiAlH_4$, this trend should also hold for larger crystallites, implying that H_2 uptake is more energetically favorable in the presence of N dopants. Notably, this is consistent with the observed difference in hydriding behavior between the CMK-3 and NCMK-3 confined materials, confirming the role of the Li adatom formation on N binding sites and resulting charge redistribution on reaction thermodynamics.

CONCLUSIONS

We demonstrate here a concept for altering the reaction pathways and energetics of chemical processes at nanoscale. The thermodynamic properties of metastable $LiAlH_4$ are significantly modified by confinement in the nanochannels of N-doped CMK-3. Our experiments and calculations reveal that the nitrogen functionalities on the NCMK-3 scaffold promote low-temperature dehydrogenation of $LiAlH_4$ to form Al particles and LiH, bypassing the stable Li_3AlH_6 intermediate phase observed in bulk. Surprisingly, the material obtained after hydrogen desorption from $LiAlH_4$@NCMK-3 can be regenerated back into $LiAlH_4$ in 80% yield, which has thus far been regarded as not feasible. DFT and AIMD modeling results indicate that the contribution of cluster cohesion energy is far weaker for $(Li_3AlH_6)_n$ than for $(LiAlH_4)_n$ clusters (n = 1−8), leading to the bypassing of the intermediate Li_3AlH_6 phase. Furthermore, it was revealed that N defect sites can lower the energy of hydriding ($\Delta E_{hydriding}$) by interacting with $LiAlH_4$ clusters more intimately than in pristine carbon, changing the DOS in the vicinity of the Fermi level and effectively acting as solvation sites for lithium ions.

Strict control over the location and orientation of metal hydride species at the nanoscale can enable the precise placement of electron acceptor species in the vicinity of electron donor species within the porous host to optimize the promotional effects observed, accelerate the H_2 sorption kinetics, and tune the energetics of chemical processes. As the results in this work indicate, the creation of such a "designed metal hydride-functionalized scaffold composite" and the optimal tuning of its properties can address important materials science challenges in energy generation and storage and can lead to a better understanding of confinement effects in nanoscale volumes.[45]

METHODS

Purification of Lithium Aluminum Hydride ($LiAlH_4$). $LiAlH_4$ was purified by recrystallization prior to use by dissolving 2.0 g of commercial $LiAlH_4$ (Sigma-Aldrich) in 25 mL of diethyl ether, followed by filtration *via* a 0.45 μm PTFE syringe filter. The clear, filtered solution was evacuated and vacuum-dried overnight in a Schlenk flask, and a fine white powder of $LiAlH_4$ was obtained. All the purification steps were conducted under an inert Ar atmosphere (<0.2 ppm of O_2 and H_2O).

Treatment of Carbon Materials under Hydrogen. Mesoporous carbons CMK-3 and N-doped CMK-3 (NCMK-3, 21 wt % nitrogen) were purchased from ACS Materials Inc. and pretreated in a reducing hydrogen environment at elevated temperatures to remove oxygen-containing surface functionalities and trapped water molecules within the pores, which can potentially react with $LiAlH_4$. The pretreatment was performed in the hydrogen cycling kinetics

https://doi.org/10.1021/acsnano.1c02079
ACS Nano XXXX, XXX, XXX−XXX

measurement mode of a PCT-Pro Sieverts type apparatus at temperatures between 350 and 380 °C. Each hydrogen cycle consists of three steps: 60 min at 20 bar H_2, 5 min under static vacuum, and 10 min under dynamic vacuum to remove volatiles. The carbon materials were treated for at least 10 cycles and subsequently transferred into an Ar glovebox for the solvent-driven infiltration.

Nanoconfinement of $LiAlH_4$. Twenty-five milligrams of purified $LiAlH_4$ was dissolved into 1.25 mL of dried diethyl ether obtained from a solvent purification system. The $LiAlH_4$ solution was filtrated by a 0.45 μm syringe filter and added to 100 mg of the pretreated mesoporous carbon scaffolds (CMK-3 and NCMK-3). The mixture was kept at or slightly below −50 °C for 1 h and evacuated at room temperature for 4 h. Finally, the evacuated samples were heated to 50 °C for 2 h to remove residual solvent in an Ar glovebox.

Hydrogen Uptake and Release. *H_2 Desorption.* The desorption of the nanoconfined $LiAlH_4$ samples was conducted with a Sievert-type apparatus (PCTPro, Setaram). The samples were heated at a ramp rate of 2 °C min^{-1} from room temperature to 240 °C and maintained at 240 °C for 4 h. The desorbed powder samples were collected under an Ar atmosphere.

High-Pressure Hydrogenation. The desorbed samples were hydrogenated in a custom high-pressure system, capable of reaching 100 MPa *via* a Newport Scientific compressor. The high-pressure vessel (Hi-Pressure 316 SS) was assembled and loaded in an Ar-containing glovebox. First, samples were loaded into stainless steel crucibles capped with frits. Up to four crucibles were then loaded into the vessel along with cylindrical stainless steel slugs to ensure the samples all rested in the main heating zone of the furnace. The closed vessel was then transported to the high-pressure system, where all gas lines were purged three times with helium prior to the vessel being opened. The vessel was purged an additional three times each with helium and hydrogen. For tests at 100 MPa and 50 °C, the system was first pressurized to 90 MPa with hydrogen to avoid overpressurization upon heating. The vessel was then heated to 50 °C, and the pressure was regularly monitored and topped off as needed to maintain the desired 100 MPa set point. The vessels were held isothermal and isobaric for 1−3 days, after which time the system was cooled to room temperature before the pressure was vented. The vessel was closed and returned to the Ar glovebox for disassembly and sample collection.

Characterization. Powder X-ray diffraction patterns were acquired on an Oxford Diffraction Supernova in capillary mode (Cu Kα radiation) using a CCD detector at 77 mm from the samples with an exposure time of 60 s. The recorded 2D images were added and integrated to generate a 1D pattern. The samples were packed into 0.7 mm diameter capillaries inside a glovebox and sealed with vacuum grease. Infrared spectra were collected inside of a Ar glovebox on an Agilent Technologies Cary-630 instrument equipped with an attenuated total reflectance unit. Before each measurement, a background spectrum was collected. Nitrogen physisorption isotherms were measured on a Quantachrome Autosorb iQ instrument at 77 K using a N_2 bath for cooling. Prior to each measurement, the sample was degassed in a vacuum for at least 6 h. All gases used for the measurements were at 99.999% purity or higher. The BET specific surface areas were obtained from the N_2 absorption isotherms in a relative pressure range of 0.05−0.20. Pore size distributions were derived using the density functional theory calculation fitting of adsorption curves with QSDFT cylinder/slit pore equilibrium kernel. X-ray photoelectron spectroscopy (XPS) data were collected using an Omicron DAR400 X-ray source and Physical Electronics 10−360 electron-energy. The X-ray source was an Al anode (PE = 1486.6 eV), and the pass energy of the analyzer was 23.5 eV. The analysis of XPS spectra was performed using the CasaXPS software. Spectra were calibrated to the adventitious C 1s peak at 285 eV. SAXS/WAXS measurements were conducted at SSRL beamline 1−5 with λ = 0.7999 Å incident energy and a 1 m sample-to-detector distance. Samples were prepared in ø 1.0 mm quartz capillaries with 10 μm thick walls in an Ar glovebox and connected to a heating cell[46] with Swagelok compression fittings. A type K thermocouple was inserted into the capillary to monitor the sample temperature. The sample cell transferred from the glovebox air-free was interfaced to a gas handling manifold where the samples were evacuated and subsequently pressurized with 4 bar H_2 backpressure for all measurements. 2D SAXS and WAXS images were processed and radially integrated with the Nika macro[47] in IgorPro.

The high-angle annular dark-field (HAADF) scanning transmission electron microscopy (STEM) images and EDX line scans in Figure 1b and Figure S6 show that the powder of $LiAlH_4$@NCMK-3 was diluted in dry toluene and a drop of sample solution was placed onto a lacey carbon TEM grid, which was dried under a vacuum overnight. The image shown in the left panel of the Figure 1b was obtained on a JEOL JEM-2100F microscope operated at 200 kV, and the image shown in the right panel of the Figure 1b was obtained on a JEOL ARM-200F aberration-corrected microscope operated at 80 kV and installed at National Center for Interuniversity Research Facility (South Korea). The samples were shortly exposed to air immediately before the sample loading. The convergence semiangle was 19 mrad, and the collection semiangle spanned from 68 to 280 mrad. EDX line scan was performed on an ARM-200F microscope with an Oxford Instruments X-Max silicon drift detector (SDD) with an active area of 100 mm and a solid angle of 0.9 sr. Transmission electron microscopy and energy dispersive X-ray spectroscopy elemental mapping in Figure 3b and Figures S7 and S10 were conducted on a ThermoFisher Titan Themis Z TEM operated at 300 kV. The samples were immersed in dry toluene and then dropcast onto Cu grids coated with a lacey carbon film. EDX data were collected with a Super-X four-quadrant SDD with a collection solid angle of approximately 0.7 sr. Data were collected with pixel times of 10−20 μs, and multiple frames were collected with drift correction for total acquisition times of approximately 10 min. Elemental maps were generated after parabolic background subtraction. X-ray absorption spectra were acquired at Beamline 8.0.1.4 at the Advanced Light Source. All samples were prepared in an Ar-filled glovebox (H_2O, O_2 < 0.1 ppm) with an UHV compatible transfer tool, allowing the samples to be mounted in the experimental chamber without ever exposing them to air. XAS measurements were carried out under UHV conditions at less than 1.0×10^{-9} Torr. XAS was conducted in surface-sensitive total electron yield mode and bulk sensitive fluorescence mode. Sieverts measurements were performed on a PCT-Pro2000 instrument (Setaram, Inc.). Approximately 150 mg of sample was transferred to the reactor connected to the instrument. Prior to each measurement, the reactor was evacuated and the volume was calibrated using He gas. Magic angle spinning nuclear magnetic resonance (MAS NMR) measurements were collected using a triple resonance probe on a 600 MHz (14 T) Bruker Biospin Avance III, operating at 156.37 and 233.24 MHz for ^{27}Al and ^{7}Li, respectively. Additional details on the specifics of MAS NMR measurements are provided in the SI (Supporting Information Note 3).

Theoretical Calculations. DFT calculations and *ab initio* molecular dynamics simulations were performed with the Vienna *ab initio* simulation package (VASP). NVT-ensemble *ab initio* molecular dynamics simulations were performed within the Born−Oppenheimer (BO) approximation with temperature regulated by the Nosé−Hoover thermostat. The N K-edge X-ray absorption (XAS) spectra were calculated using the quantum espresso source code package with the Shirley reduced basis for efficient Brillouin zone sampling. Standard PBE-GGA approximation was used to estimate the exchange-correlation functional in DFT (additional details are shown in Supporting Information Note 4).

ASSOCIATED CONTENT

Supporting Information

The Supporting Information is available free of charge at https://pubs.acs.org/doi/10.1021/acsnano.1c02079.

Figures of pore size distributions, FTIR spectra, PXRD patterns, ^{7}Li MAS NMR spectra, N 1s spectra, schematic illustration of N-functionalities, brightness analysis, HAADF-STEM line profile, EDS signals, EELS profile,

https://doi.org/10.1021/acsnano.1c02079
ACS Nano XXXX, XXX, XXX−XXX

hydrogen desorption kinetic curve, high-angle annular dark field EDS map image, relaxed geometries, schematic representation of spontaneous interdiffusion, optimized structures of graphene sheets, *ex situ* N K-edge soft TEY X-ray absorption spectra, isosurface of charge density difference, and electronic density of states, tables of BET surface areas and total pore volumes, relative amount of various nitrogen functionalities, and NMR parameters, and notes of synthesis and storage methods, identification of the origin of partial $LiAlH_4$ decomposition upon solvent infiltration, detailed description of MAS NMR measurements, and detailed description of theoretical calculations (PDF)

AUTHOR INFORMATION

Corresponding Authors

Brandon C. Wood − *Lawrence Livermore National Laboratory, Livermore, California 94550, United States;* orcid.org/0000-0002-1450-9719; Email: wood37@llnl.gov

Eun Seon Cho − *Department of Chemical and Biomolecular Engineering (BK21+ Program), Korea Advanced Institute of Science and Technology (KAIST), Daejeon 34141, Republic of Korea;* orcid.org/0000-0001-9428-1269; Email: escho@kaist.ac.kr

Vitalie Stavila − *Sandia National Laboratories, Livermore, California 94550, United States;* orcid.org/0000-0003-0981-0432; Email: vnstavi@sandia.gov

Authors

YongJun Cho − *Sandia National Laboratories, Livermore, California 94550, United States; Department of Chemical and Biomolecular Engineering (BK21+ Program), Korea Advanced Institute of Science and Technology (KAIST), Daejeon 34141, Republic of Korea*

Sichi Li − *Lawrence Livermore National Laboratory, Livermore, California 94550, United States;* orcid.org/0000-0002-2565-5906

Jonathan L. Snider − *Sandia National Laboratories, Livermore, California 94550, United States*

Maxwell A. T. Marple − *Lawrence Livermore National Laboratory, Livermore, California 94550, United States;* orcid.org/0000-0001-5251-8301

Nicholas A. Strange − *SLAC National Accelerator Laboratory, Menlo Park, California 94025, United States;* orcid.org/0000-0001-5699-7274

Joshua D. Sugar − *Sandia National Laboratories, Livermore, California 94550, United States*

Farid El Gabaly − *Sandia National Laboratories, Livermore, California 94550, United States;* orcid.org/0000-0002-5822-9938

Andreas Schneemann − *Sandia National Laboratories, Livermore, California 94550, United States;* orcid.org/0000-0001-6801-2735

Sungsu Kang − *Center for Nanoparticle Research, Institute for Basic Science (IBS), Seoul 08826, Republic of Korea; School of Chemical and Biological Engineering and Institute of Chemical Process, Seoul National University, Seoul 08826, Republic of Korea*

Min-ho Kang − *Center for Nanoparticle Research, Institute for Basic Science (IBS), Seoul 08826, Republic of Korea; School of Chemical and Biological Engineering and Institute of Chemical Process, Seoul National University, Seoul 08826, Republic of Korea*

Hayoung Park − *Center for Nanoparticle Research, Institute for Basic Science (IBS), Seoul 08826, Republic of Korea; School of Chemical and Biological Engineering and Institute of Chemical Process, Seoul National University, Seoul 08826, Republic of Korea*

Jungwon Park − *Center for Nanoparticle Research, Institute for Basic Science (IBS), Seoul 08826, Republic of Korea; School of Chemical and Biological Engineering and Institute of Chemical Process, Seoul National University, Seoul 08826, Republic of Korea;* orcid.org/0000-0003-2927-4331

Liwen F. Wan − *Lawrence Livermore National Laboratory, Livermore, California 94550, United States;* orcid.org/0000-0002-5391-0804

Harris E. Mason − *Lawrence Livermore National Laboratory, Livermore, California 94550, United States;* orcid.org/0000-0002-1840-0550

Mark D. Allendorf − *Sandia National Laboratories, Livermore, California 94550, United States;* orcid.org/0000-0001-5645-8246

Complete contact information is available at: https://pubs.acs.org/10.1021/acsnano.1c02079

Author Contributions

V.S., B.C.W., and E.S.C. conceived and coordinated the project. Y.C. performed the synthesis of nanoconfined materials with help from J.L.S. and A.S. M.A.T.M. and H.E.M. performed the solid-state NMR measurements. Y.C., V.S., F.E.G., J.L.S., and N.A.S. carried out the XRD, XAS, XPS, and SAXS measurements. J.D.S., S.K., M.K., H.P., and J.P performed the TEM, EELS, and EDS experiments. S.L., L.F.W., and B.C.W. performed the *ab initio* simulations. Y.C., S.L, B.C.W, E.S.C., M.D.A., and V.S. wrote the manuscript and prepared the figures with help from the other coauthors. All the authors contributed to the scientific discussions, data analysis, and preparation of the manuscript.

Notes

The data sets generated during the current study are available from the corresponding authors on request.
The authors declare no competing financial interest.

ACKNOWLEDGMENTS

This paper has been previously submitted to a preprint server. Cho, Y.; Li, S.; Marple, M.; Strange, N.; Sugar, J.; Gabaly, F.; Schneemann, A.; Kang, S.; Kang, M.; Park, H.; Park, J.; Wan, L.; Mason, H.; Allendorf, M.; Wood, B.; Cho, E.; Stavila, V. *Reversing the Irreversible: Thermodynamic Stabilization of Lithium Aluminum Hydride Nanoconfined Within a Nitrogen-Doped Carbon Host*. Research square: https://assets.researchsquare.com/files/rs-141693/v1/1cfb04ff-9436-400f-9d68-ecba8e36b529.pdf (Jan 29, 2021). Sandia National Laboratories is a multimission laboratory managed and operated by National Technology and Engineering Solutions of Sandia, LLC., a wholly owned subsidiary of Honeywell International, Inc., for the U.S. Department of Energy's National Nuclear Security Administration under contract DE-NA-0003525. The authors gratefully acknowledge funding from the U.S. Department of Energy, Office of Energy Efficiency and Renewable Energy, Hydrogen and Fuel Cell Technologies Office, through the Hydrogen Storage Materials Advanced Research Consortium (HyMARC). This research

https://doi.org/10.1021/acsnano.1c02079
ACS Nano XXXX, XXX, XXX−XXX

was supported by the Laboratory Directed Research and Development (LDRD) program at Sandia National Laboratories. This work was also supported by the International Energy Joint R&D Program of the Korea Institute of Energy Technology Evaluation and Planning (KETEP), granted financial resource from the Ministry of Trade, Industry & Energy, Republic of Korea (No. 20188520000570). The computational portion of the work was performed under the auspices of the DOE by Lawrence Livermore National Laboratory (LLNL) under Contract DE-AC52-07NA27344, with computing support from the LLNL Institutional Computing Grand Challenge program. This research used resources from the Advanced Light Source, which is a DOE Office of Science User Facility under contract no. DE-AC02-05CH11231. Any subjective views or opinions that might be expressed in the paper do not necessarily represent the views of the U.S. Department of Energy or the United States Government.

REFERENCES

(1) Aykol, M.; Dwaraknath, S. S.; Sun, W.; Persson, K. A. Thermodynamic Limit for Synthesis of Metastable Inorganic Materials. *Science Adv.* **2018**, *4*, eaaq0148.

(2) Ye, L.; Fitzhugh, W.; Gil-González, E.; Wang, Y.; Su, Y.; Su, H.; Qiao, T.; Ma, L.; Zhou, H.; Hu, E.; Li, X. Toward Higher Voltage Solid-State Batteries by Metastability and Kinetic Stability Design. *Adv. Energy Mater.* **2020**, *10*, 2001569.

(3) Ratha, S.; Samantara, A. K.; Singha, K. K.; Gangan, A. S.; Chakraborty, B.; Jena, B. K.; Rout, C. S. Urea-Assisted Room Temperature Stabilized Metastable β-$NiMoO_4$: Experimental and Theoretical Insights into Its Unique Bifunctional Activity toward Oxygen Evolution and Supercapacitor. *ACS Appl. Mater. Interfaces* **2017**, *9*, 9640−9653.

(4) Tasnádi, F.; Alling, B.; Höglund, C.; Wingqvist, G.; Birch, J.; Hultman, L.; Abrikosov, I. A. Origin of the Anomalous Piezoelectric Response in Wurtzite $Sc_xAl_{1-x}N$ Alloys. *Phys. Rev. Lett.* **2010**, *104*, 137601.

(5) Vidal, J.; Lany, S.; Francis, J.; Kokenyesi, R.; Tate, J. Structural and Electronic Modification of Photovoltaic SnS by Alloying. *J. Appl. Phys.* **2014**, *115*, 113507.

(6) Zhang, Z.; Zandkarimi, B.; Alexandrova, A. N. Ensembles of Metastable States Govern Heterogeneous Catalysis on Dynamic Interfaces. *Acc. Chem. Res.* **2020**, *53*, 447−458.

(7) Kumar, R.; Karkamkar, A.; Bowden, M.; Autrey, T. Solid-State Hydrogen Rich Boron−Nitrogen Compounds for Energy Storage. *Chem. Soc. Rev.* **2019**, *48*, 5350−5380.

(8) Graetz, J.; Wegrzyn, J.; Reilly, J. J. Regeneration of Lithium Aluminum Hydride. *J. Am. Chem. Soc.* **2008**, *130*, 17790−17794.

(9) Zidan, R.; Garcia-Diaz, B. L.; Fewox, C. S.; Stowe, A. C.; Gray, J. R.; Harter, A. G. Aluminium Hydride: A Reversible Material for Hydrogen Storage. *Chem. Commun.* **2009**, *25*, 3717−3719.

(10) Schüth, F.; Bogdanović, B.; Felderhoff, M. Light Metal Hydrides and Complex Hydrides for Hydrogen Storage. *Chem. Commun.* **2004**, *20*, 2249−2258.

(11) Ni, C.; Yang, L.; Muckerman, J. T.; Graetz, J. N-Alkylpyrrolidine· Alane Compounds for Energy Applications. *J. Phys. Chem. C* **2013**, *117*, 2628−2634.

(12) Lacina, D.; Yang, L.; Chopra, I.; Muckerman, J.; Chabal, Y.; Graetz, J. Investigation of $LiAlH_4$−THF Formation by Direct Hydrogenation of Catalyzed Al and LiH. *Phys. Chem. Chem. Phys.* **2012**, *14*, 6569−6576.

(13) Wang, J.; Ebner, A. D.; Ritter, J. A. Physiochemical Pathway for Cyclic Dehydrogenation and Rehydrogenation of $LiAlH_4$. *J. Am. Chem. Soc.* **2006**, *128*, 5949−5954.

(14) Wong, B. M.; Lacina, D.; Nielsen, I. M.; Graetz, J.; Allendorf, M. D. Thermochemistry of Alane Complexes for Hydrogen Storage: A Theoretical and Experimental Investigation. *J. Phys. Chem. C* **2011**, *115*, 7778−7786.

(15) Ni, C.; Wegrzyn, J. E.; Zhou, W.; Celebi, Y.; Graetz, J. N-Alkylpiperidine-Alane Compounds and Their Applications in Alane Regeneration. *Int. J. Hydrogen Energy* **2013**, *38*, 9779−9785.

(16) Schneemann, A.; White, J. L.; Kang, S.; Jeong, S.; Wan, L. W. F.; Cho, E. S.; Heo, T. W.; Prendergast, D.; Urban, J. J.; Wood, B. C.; Allendorf, M. D.; Stavila, V. Nanostructured Metal Hydrides for Hydrogen Storage. *Chem. Rev.* **2018**, *118*, 10775−10839.

(17) Gunda, H.; Klebanoff, L. E.; Sharma, P. A.; Varma, A. K.; Dolia, V.; Jasuja, K.; Stavila, V. Progress, Challenges, and Opportunities in the Synthesis, Characterization, and Application of Metal-Boride-Derived Two-Dimensional Nanostructures. *ACS Mater. Lett.* **2021**, *3*, 535−556.

(18) Leick, N.; Strange, N. A.; Schneemann, A.; Stavila, V.; Gross, K.; Washton, N.; Settle, A.; Martinez, M. B.; Gennett, T.; Christensen, S. T. Al_2O_3 Atomic Layer Deposition on Nanostructured γ-$Mg(BH_4)_2$ for H_2 Storage. *ACS Appl. Energy Mater.* **2021**, *4*, 1150−1162.

(19) Wood, B. C.; Stavila, V.; Poonyayant, N.; Heo, T. W.; Ray, K. G.; Klebanoff, L. E.; Udovic, T. J.; Lee, J. R. I.; Angboonpong, N.; Sugar, J. D.; Pakawatpanurut, P. Nanointerface-Driven Reversible Hydrogen Storage in the Nanoconfined Li-N-H System. *Adv. Mater. Interfaces* **2017**, *4*, 1600803.

(20) Schneemann, A.; Wan, L. F.; Lipton, A. S.; Liu, Y.-S.; Snider, J. L.; Baker, A. A.; Sugar, J. D.; Spataru, C. D.; Guo, J.; Autrey, T. S.; et al. Nanoconfinement of Molecular Magnesium Borohydride Captured in a Bipyridine-Functionalized Metal−Organic Framework. *ACS Nano* **2020**, *14*, 10294−10304.

(21) Jeong, S.; Heo, T. W.; Oktawiec, J.; Shi, R.; Kang, S.; White, J. L.; Schneemann, A.; Zaia, E. W.; Wan, L. F.; Ray, K. G.; et al. A Mechanistic Analysis of Phase Evolution and Hydrogen Storage Behavior in Nanocrystalline $Mg(BH_4)_2$ within Reduced Graphene Oxide. *ACS Nano* **2020**, *14*, 1745−1756.

(22) Wan, L. F.; Cho, E. S.; Marangoni, T.; Shea, P.; Kang, S.; Rogers, C.; Zaia, E.; Cloke, R. R.; Wood, B. C.; Fischer, F. R.; et al. Edge-Functionalized Graphene Nanoribbon Encapsulation to Enhance Stability and Control Kinetics of Hydrogen Storage Materials. *Chem. Mater.* **2019**, *31*, 2960−2970.

(23) Nielsen, T. K.; Besenbacher, F.; Jensen, T. R. Nanoconfined Hydrides for Energy Storage. *Nanoscale* **2011**, *3*, 2086−2098.

(24) Jeon, K.-J.; Moon, H. R.; Ruminski, A. M.; Jiang, B.; Kisielowski, C.; Bardhan, R.; Urban, J. J. Air-Stable Magnesium Nanocomposites Provide Rapid and High-Capacity Hydrogen Storage without Using Heavy-Metal Catalysts. *Nat. Mater.* **2011**, *10*, 286−291.

(25) Chong, L.; Zeng, X.; Ding, W.; Liu, D.-J.; Zou, J. $NaBH_4$ in "Graphene Wrapper:" Significantly Enhanced Hydrogen Storage Capacity and Regenerability through Nanoencapsulation. *Adv. Mater.* **2015**, *27*, 5070−5074.

(26) Cho, E. S.; Ruminski, A. M.; Aloni, S.; Liu, Y.-S.; Guo, J.; Urban, J. J. Graphene Oxide/Metal Nanocrystal Multilaminates as the Atomic Limit for Safe and Selective Hydrogen Storage. *Nat. Commun.* **2016**, *7*, 10804.

(27) White, J. L.; Strange, N. A.; Sugar, J. D.; Snider, J. L.; Schneemann, A.; Lipton, A. S.; Toney, M. F.; Allendorf, M. D.; Stavila, V. Melting of Magnesium Borohydride under High Hydrogen Pressure: Thermodynamic Stability and Effects of Nanoconfinement. *Chem. Mater.* **2020**, *32*, 5604−5615.

(28) de Jongh, P. E.; Allendorf, M.; Vajo, J. J.; Zlotea, C. Nanoconfined Light Metal Hydrides for Reversible Hydrogen Storage. *MRS Bull.* **2013**, *38*, 488−494.

(29) Nielsen, T. K.; Polanski, M.; Zasada, D.; Javadian, P.; Besenbacher, F.; Bystrzycki, J.; Skibsted, J.; Jensen, T. R. Improved Hydrogen Storage Kinetics of Nanoconfined $NaAlH_4$ Catalyzed with $TiCl_3$ Nanoparticles. *ACS Nano* **2011**, *5*, 4056−4064.

(30) Carr, C. L.; Jayawardana, W.; Zou, H.; White, J. L.; El Gabaly, F.; Conradi, M. S.; Stavila, V.; Allendorf, M. D.; Majzoub, E. H. Anomalous H_2 Desorption Rate of $NaAlH_4$ Confined in Nitrogen-

https://doi.org/10.1021/acsnano.1c02079
ACS Nano XXXX, XXX, XXX−XXX

Doped Nanoporous Carbon Frameworks. *Chem. Mater.* **2018**, *30*, 2930−2938.
(31) Carr, C. L.; Majzoub, E. H. Surface-Functionalized Nanoporous Carbons for Kinetically Stabilized Complex Hydrides through Lewis Acid−Lewis Base Chemistry. *J. Phys. Chem. C* **2016**, *120*, 11426−11432.
(32) Liu, X.; McGrady, G. S.; Langmi, H. W.; Jensen, C. M. Facile Cycling of Ti-Doped $LiAlH_4$ for High Performance Hydrogen Storage. *J. Am. Chem. Soc.* **2009**, *131*, 5032−5033.
(33) Liu, S. S.; Li, Z. B.; Jiao, C. L.; Si, X. L.; Yang, L. N.; Zhang, J.; Zhou, H. Y.; Huang, F. L.; Gabelica, Z.; Schick, C.; Sun, L. X.; Xu, F. Improved Reversible Hydrogen Storage of $LiAlH_4$ by Nano-Sized TiH_2. *Int. J. Hydrogen Energy* **2013**, *38*, 2770−2777.
(34) Ares, J. R.; Aguey-Zinsou, K. F.; Porcu, M.; Sykes, J. M.; Dornheim, A.; Klassen, T.; Bormann, R. Thermal and Mechanically Activated Decomposition of $LiAlH_4$. *Mater. Res. Bull.* **2008**, *43*, 1263−1275.
(35) Ke, X.; Chen, C. Thermodynamic Functions and Pressure-Temperature Phase Diagram of Lithium Alanates by *ab Initio* Calculations. *Phys. Rev. B: Condens. Matter Mater. Phys.* **2007**, *76*, 024112.
(36) Thommes, M.; Kaneko, K.; Neimark, A. V.; Olivier, J. P.; Rodriguez-Reinoso, F.; Rouquerol, J.; Sing, K. S. Physisorption of Gases, with Special Reference to the Evaluation of Surface Area and Pore Size Distribution (IUPAC Technical Report). *Pure Appl. Chem.* **2015**, *87*, 1051−1069.
(37) Stavila, V.; Bhakta, R. K.; Alam, T. M.; Majzoub, E. H.; Allendorf, M. D. Reversible Hydrogen Storage by $NaAlH_4$ Confined within a Titanium-Functionalized MOF-74 (Mg) Nanoreactor. *ACS Nano* **2012**, *6*, 9807−9817.
(38) Wang, L.; Rawal, A.; Quadir, M. Z.; Aguey-Zinsou, K. F. Nanoconfined Lithium Aluminium Hydride ($LiAlH_4$) and Hydrogen Reversibility. *Int. J. Hydrogen Energy* **2017**, *42*, 14144−14153.
(39) Zhao, Y. R.; Han, M.; Wang, H. X.; Chen, C. C.; Chen, J. $LiAlH_4$ Supported on TiO_2/Hierarchically Porous Carbon Nanocomposites with Enhanced Hydrogen Storage Properties. *Inorg. Chem. Front.* **2016**, *3*, 1536−1542.
(40) Ngene, P.; Verkuijlen, M. H. W.; Barre, C.; Kentgens, A. P. M.; de Jongh, P. E. Reversible Li-Insertion in Nanoscaffolds: A Promising Strategy to Alter the Hydrogen Sorption Properties of Li-Based Complex Hydrides. *Nano Energy* **2016**, *22*, 169−178.
(41) Wahab, M. A.; Beltramini, J. N. Catalytic Nanoconfinement Effect of *in-Situ* Synthesized Ni-Containing Mesoporous Carbon Scaffold (Ni-MCS) on the Hydrogen Storage Properties of $LiAlH_4$. *Int. J. Hydrogen Energy* **2014**, *39*, 18280−18290.
(42) Wiench, J.; Balema, V.; Pecharsky, V.; Pruski, M. Solid-State ^{27}Al NMR Investigation of Thermal Decomposition of $LiAlH_4$. *J. Solid State Chem.* **2004**, *177*, 648−653.
(43) Bhakta, R.; Maharrey, S.; Stavila, V.; Highley, A.; Alam, T.; Majzoub, E.; Allendorf, M. Thermodynamics and Kinetics of $NaAlH_4$ Nanocluster Decomposition. *Phys. Chem. Chem. Phys.* **2012**, *14*, 8160−8169.
(44) Wood, B. C.; Ogitsu, T.; Otani, M.; Biener, J. First-Principles-Inspired Design Strategies for Graphene-Based Supercapacitor Electrodes. *J. Phys. Chem. C* **2014**, *118*, 4−15.
(45) Meldrum, F. C.; O'Shaughnessy, C. Crystallization in Confinement. *Adv. Mater.* **2020**, *32*, 2001068.
(46) Hoffman, A. S.; Singh, J. A.; Bent, S. F.; Bare, S. R. *In Situ* Observation of Phase Changes of a Silica-Supported Cobalt Catalyst for the Fischer−Tropsch Process by the Development of a Synchrotron-Compatible *in Situ*/*Operando* Powder X-Ray Diffraction Cell. *J. Synchrotron Radiat.* **2018**, *25*, 1673−1682.
(47) Ilavsky, J. Nika: Software for Two-Dimensional Data Reduction. *J. Appl. Crystallogr.* **2012**, *45*, 324−328.
(48) Jun, S.; Joo, S. H.; Ryoo, R.; Kruk, M.; Jaroniec, M.; Liu, Z.; Ohsuna, T.; Terasaki, O. Synthesis of New, Nanoporous Carbon with Hexagonally Ordered Mesostructure. *J. Am. Chem. Soc.* **2000**, *122*, 10712−10713.
(49) Block, J.; Gray, A. The Thermal Decomposition of Lithium Aluminum Hydride. *Inorg. Chem.* **1965**, *4*, 304−305.

https://doi.org/10.1021/acsnano.1c02079
ACS Nano XXXX, XXX, XXX−XXX